

Controlling defects of laser-powder bed fusion processed 316L stainless steel via ultrasonic nanocrystalline surface modification

Rae Eon Kim^a, Sang Guk Jeong^b, Hyojeong Ha^b, Do Won Lee^b, Auezhan Amanov^c, Hyoung Seop Kim^{a,b,d,*}

^a*Graduate Institute of Ferrous & Energy Materials Technology, Pohang University of Science and Technology (POSTECH), Pohang 37673, Republic of Korea*

^b*Department of Materials Science and Engineering, Pohang University of Science and Technology (POSTECH), Pohang 37673, Republic of Korea*

^c*Department of Mechanical Engineering, Sun Moon University, Asan 31460, Republic of Korea*

^d*Advanced Institute for Materials Research (WPI-AIMR), Tohoku University, Sendai, 980-8577, Japan*

*Corresponding author: Tel.: +82 54 279 2150; E-mail: hskim@postech.ac.kr

Abstract

Metal additive manufacturing (MAM) offers an excellent capability for designing complex geometries with topology-optimized and near-net-shaped structures. The optimization-designed MAM parts with constrained volume require superior mechanical properties to broaden their utilization in the industry. However, the intrinsic defects generated during the building process deteriorate the mechanical functionality and limit utilization in various industrial applications. In this study, we propose a new strategy to reduce generated defects using ultrasonic nanocrystal surface modification (UNSM) on laser powder bed fusion (LPBF) processed 316L stainless steel. Subsurface pores and high surface roughness in MAM parts were significantly improved through the impact of UNSM treatment, and a gradient structure with mechanical incompatibility was developed. Consequently, the LPBF-processed samples after UNSM treatment show an excellent combination of strength and ductility, which is attributed to the high synergistic hardening from the gradient microstructure and the suppression of damage evolution by controlling built defects.

Keywords: Laser powder bed fusion; Gradient structure; Defects; Ultrasonic nanocrystal surface modification; Austenitic stainless steels

Main text

1. Introduction

Metal additive manufacturing (MAM) is a leading manufacturing technology with excellent capabilities for fabricating customized parts with geometrically complex structures [1]. Among the various techniques for MAM, laser-powder bed fusion (LPBF) has attracted significant attention owing to its high resolution for building parts and achieving high mechanical performance [2]. As LPBF produces parts in a layer-by-layer fashion through cycles of powder spreading and laser selective scanning, it can produce components with geometrically complex structures such as near-net shapes [3]. Therefore, MAM enables a maximum weight reduction strategy with near-net shape and topology optimization, which is challenging in conventional manufacturing [4, 5]. The lightweight structure of LPBF-processed parts considerably reduces the cross-sectional area subjected to the load during service. The lightweight components in industrial applications require superior mechanical properties to ensure structural safety during service [6]. However, the building defects inherent in LPBF processing from selective laser melting and solidification have a greater influence on the MAM parts when employing the weight reduction strategy [7].

Undesirable defects, including porosity and high surface roughness, are critical quality inhibitors in MAM parts, leading to a deterioration of the mechanical functionality of the parts [8, 9]. The pores during building come from various sources: the entrapment of gas during rapid solidification (gas pores), unstable vapor due to excessive energy density (keyhole), and the insufficient overlap of melt pools (lack of fusion) [10]. Furthermore, the source of pores can be attributed to the feedstock itself, where existing pores in powders [11] and contamination from the environment play a role [12]. Although the porosity of LPBF parts can be alleviated through great effort in optimizing processing parameters, it is difficult to completely control the porosity in LPBF parts. In addition, rough surfaces in LPBF parts are inevitable due to their layer-by-layer fabrication, partially-melted powder, agglomeration, and splashing particles [13]. Highly rough surfaces act as crack initiation sites, possibly resulting in inferior mechanical properties of the MAM parts [14, 15].

The MAM-built defects can be addressed through polishing/grinding or hot isostatic pressing (HIP) [16, 17]. While surface polishing/grinding improves surface roughness, it still has limitations in addressing volumetric defects such as pores. On the other hand, the high temperature and pressure during HIP can effectively decrease internal pores, but it does not refine the high surface roughness of the LPBF samples [18]. Furthermore, HIP can deteriorate the mechanical properties of LPBF parts because excessive heating during HIP eliminates the unique microstructures in LPBF materials, such as fine grain size and high dislocation density [19]. Therefore, in this work, to control defects in MAM parts, the new approach of ultrasonic nanocrystalline surface modification (UNSM) was employed on LPBF-processed samples.

The UNSM treatment involves striking the surface of the substrate with a tungsten carbide horn at ultrahigh frequencies, inducing surface severe plastic deformation. The UNSM can greatly enhance mechanical properties by developing a gradient microstructure within the substrate [20-22]. Furthermore, the UNSM-modified surface improves wear resistance, surface roughness, and fatigue strength [23-26]. The surface severe plastic deformation including UNSM has been generally conducted on the machined surface of the substrate to develop a nanocrystalline gradient structure [27-30]. To date, evaluating the mechanical properties of MAM has been generally conducted on machined surfaces without considering the effect of surface defects [31-34]. However, LPBF processing creates unavoidable surface defects, and mechanical testing on the as-built part itself is needed to consider the characteristics of LPBF processing.

In this work, as-built samples fabricated by LPBF were UNSM treated to control the built defects. The high external impact during the UNSM process levels the surface elevation [35]. Moreover, the severe external impact may close the porous materials, leading to more fully dense materials, especially in thin samples. Therefore, the new methodology of UNSM treatment was investigated to overcome the intrinsic defects of MAM parts, thereby achieving further superior strength-ductility.

2. Experimental procedure

The commercial 316L stainless steel powders fabricated by gas atomization in MK Inc. were used for LPBF processing. Figure 1 shows the spherical morphology and the distribution of particle size of 316L stainless steel powders with an average particle size of 29.7 μm , which is suitable for LPBF processing. The LPBF-built samples with a thickness of 1.2 mm were

fabricated. The LPBF process was performed on a GE Concept laser (M2 Series 5) using optimized processing parameters as listed in Table 1 [36]. The laser scan strategy involved 67° rotations at each layer with bidirectional laser scanning. The laser scanning path was divided into a contour scan and a filling scan. During the LPBF process, discontinuous scanning of a filling scan at the surface produces a bumpy surface. Therefore, an additional laser line scan on the outer surface (i.e., contour scan) was conducted to ensure dimensional accuracy and surface roughness [37].

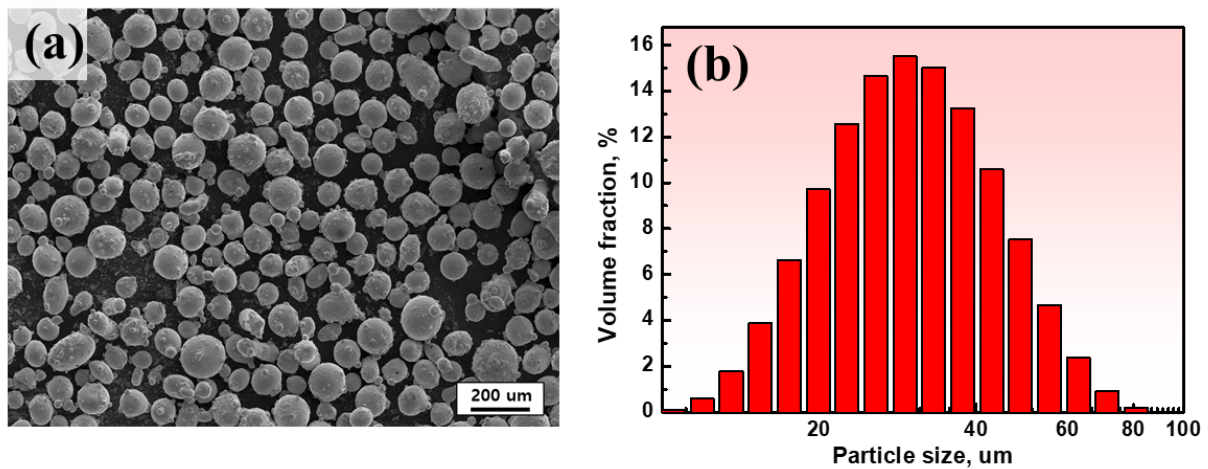


Fig. 1. (a) SEM micrograph and (b) particle size distribution of 316L stainless steel powders.

Table 1. Processing parameters for LPBF.

Parameter	Filling scan	Contour scan
Laser power (W)	370	120
Laser scanning speed (mm/s)	1350	220
Laser spot size (μm)	130	50
Hatch spacing (μm)	0.09	-
Layer thickness (mm)	0.05	-

The UNSM treatment was performed on both sides of the built samples using the processing conditions in Table 2 (Fig. 2). UNSM strikes the substrate with a WC tip of a 2.38

mm ball diameter at a high frequency along the building direction. To analyze the effect of UNSM treatment on the defects of the built materials, UNSM treatment was conducted on the as-built samples without any post-processing such as machining. After UNSM treatment, the sample thickness was reduced from 1.20 mm to 1.14 mm. For comparison, the as-built samples were polished until 1200 grit silicon carbide paper on both surfaces normal to the Y direction (Fig. 2). The three main samples investigated in this work were as follows: as-built LPBF samples (as-built), polished as-built samples (as-polished), and UNSM-treated as-built samples (UNSM-treated). The surface roughness was measured using a surface profilometer (SJ-210) with a scan speed of 0.25 mm/s and a scan length of 2.4 mm.

Table 2. Processing conditions for the UNSM treatment.

Frequency	Amplitude	Load	Feed-rate
20 kHz	30 μm	30 N	0.03 mm/rev

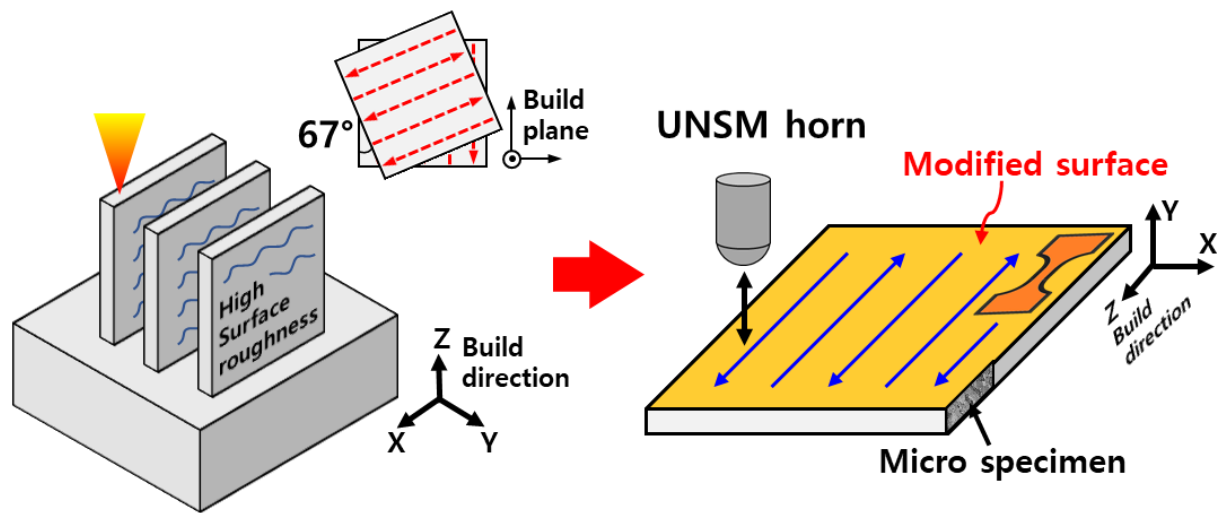


Fig. 2. A schematic showing a fabricating procedure for the UNSM-treated samples.

Vickers microhardness was measured with an FM-700 tester to establish hardness variation as a function of distance from the surface. The hardness test was conducted under a load of 100 gf and a dwell time of 10 s. Three indentations were made at each depth, and the average values were plotted. Uniaxial tensile tests were conducted with Instron 5582 at a quasi-static strain rate of 10^{-3} s^{-1} . The tensile samples were extracted along the building direction with

a flat dog-bone shape, having a gauge length of 1.5 mm and a gauge width of 1 mm (Fig. 2). The tensile testing was performed three times with digital image correlation (ARAMIS v6.1, GOM Optical Measuring Techniques) to measure the precise strain. Loading-unloading-reloading (LUR) tests were conducted at a strain rate of 10^{-3} s^{-1} to quantify the hetero-deformation-induced (HDI) strengthening of the UNSM-treated sample. Details of the method to calculate the HDI stress are available in Ref. [38].

The relative density of each sample was measured at least five times using Archimedes' method with Mettler Toledo equipment. The initial surface morphology and fractography for each specimen were observed with a field-emission scanning electron microscope (FE-SEM, JEOL-2100F). X-ray diffraction (XRD, D8-Davinci) was performed with a step size of 0.01° and a scan speed of $0.3^\circ/\text{min}$. The residual stress was investigated by an X-ray diffraction tester (XTRESS3000 diffractometer) on the (311) plane.

To evaluate the porosity in each sample, the samples were prepared with polishing using 1200 grit abrasive papers and 3, 1 μm diamond suspension, and optical microscopes (OM, BX51 M, Olympus) were used for observations. For microstructural analysis of the cross-section on the normal plane to the X direction (Fig. 2), the specimens were mechanically polished with 1200 SiC papers, followed by electropolishing with an electrolyte of 10% CH_3COOH and 90% HClO_4 . FE-SEM (FEG-XL30S) with an electron backscatter diffraction (EBSD) detector and FE-SEM (JEM-2100F) with a back-scattered electron (BSE) detector were used for microstructural characterization. The step size for taking EBSD images was 150 nm. The EBSD data were analyzed using TSL OIM analysis 7 software.

3. Results and discussion

The OM images for building defects of the present samples are shown in Fig. 3. The as-built sample presents a rough surface, whereas the as-polished and UNSM-treated samples exhibited a smooth surface (Fig. 3a-c). The results of surface roughness measurement show large roughness in the as-built samples with an average surface roughness (R_a : $\sim 8.01 \mu\text{m}$) while a significant improvement in surface roughness in the as-polished (R_a : $\sim 0.02 \mu\text{m}$) and the UNSM-treated samples (R_a : $\sim 1.07 \mu\text{m}$), as shown in Fig. S1. It indicates that both the post-processing of polishing and UNSM treatment effectively smoothed the rugged surface of the LPBF sample. It is worth noting that the as-built and as-polished samples exhibited a high number of pores near the surface. Plessis et al. [39] through X-ray microtomography ($\mu\text{-CT}$)

reported that the pores in the LPBF-processed stainless steel parts are mainly distributed near the surface. The near subsurface pores are attributed to the high energy density in the contour process. The energy density during LPBF processing can be calculated using the following equation:

$$E=P/vht, \quad (1)$$

where E , P , v , h , and t represent volumetric energy density, laser power, scan speed, hatch spacing, and layer thickness, respectively. The calculated energy densities for the filling and contour process are 61 J/mm^3 and 121 J/mm^3 , respectively (Table 1). The energy density in the contour process was approximately twofold that in the filling process because high energy density will assure the surface quality and dimensional precision. However, the high energy density used for contour processing results in deep and narrow melt pools, leading to gas entrapment and the generation of pores [40].

Figure 3d shows the porosity obtained from Fig. 3a-c. The subsurface pores are distributed until a depth of $\sim 200 \text{ }\mu\text{m}$ on both sides of as-built samples (Fig. 3a). The present surface polishing to improve surface roughness is insufficient to remove the surface porosity completely, as shown in Fig. 3b, d. However, interestingly, the UNSM-treated samples were nearly fully dense without pores at the surface region (Fig. 3c, d). More clearly, the relative densities for each sample are presented in Fig. 3e. The UNSM-treated sample has the highest value of relative density ($\rho = \sim 98.4\%$), followed by the as-polished sample ($\rho = \sim 97.8\%$), and finally the as-built sample ($\rho = \sim 97.4\%$). The UNSM tip strikes the surface at high frequencies. Therefore, the external impact from the UNSM treatment compresses the empty spaces and closes pores mechanically, making them into fully dense materials. Consequently, the UNSM treatment shows effective improvement in surface roughness and closure of pores, which are the intrinsic defects in LPBF processing.

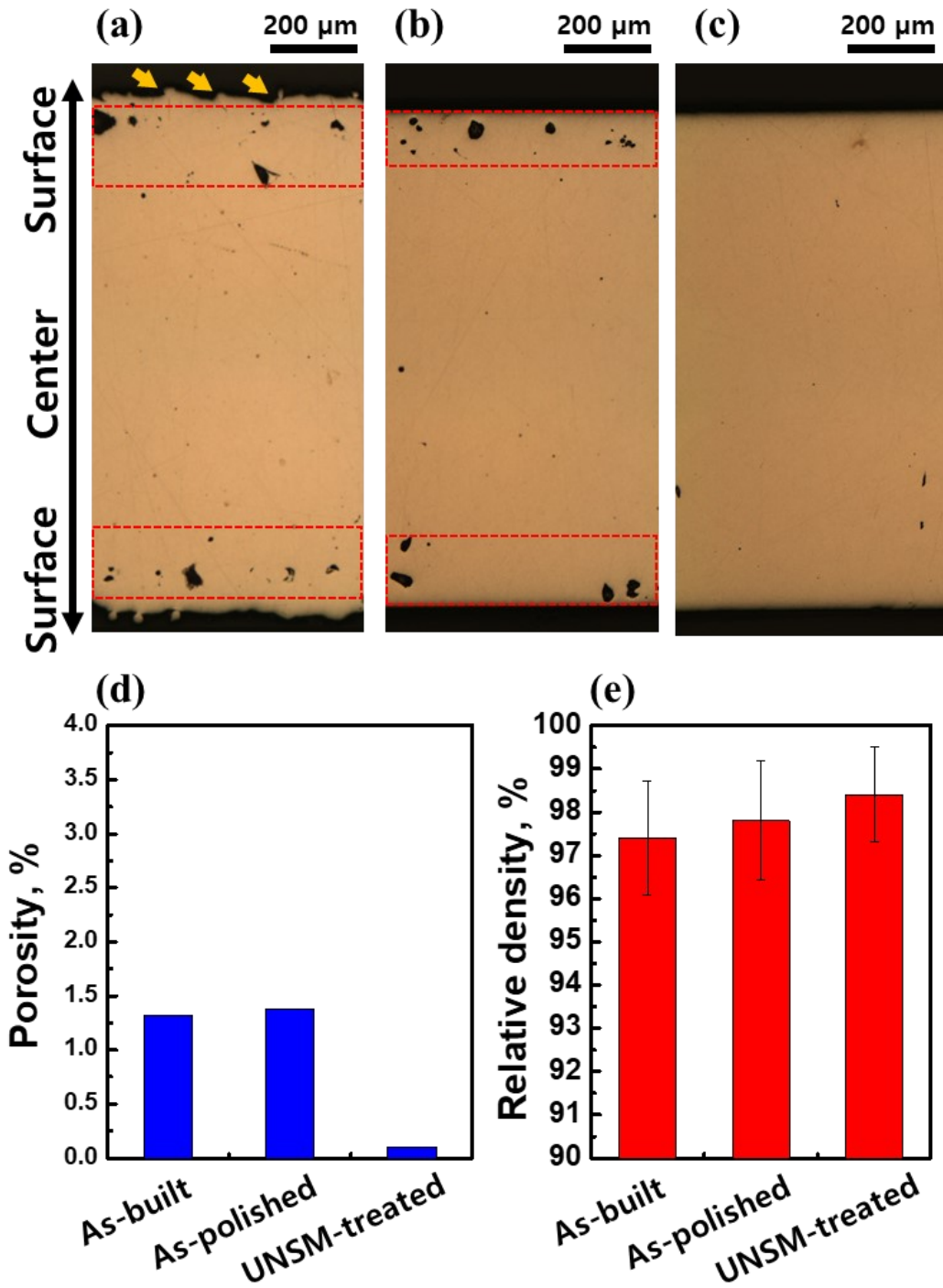


Fig. 3. OM images of the (a) as-built (b) as-polished, and (c) UNSM-treated samples. Bar charts showing (d) porosity and (e) relative density for all the samples. The yellow arrows and red dot boxes in (a, b) represent high surface roughness and pores, respectively.

The surface morphologies of the present samples were observed using SEM, as shown

in Fig. 4. Partially unmelted powder particles and micro-cracks were widely distributed on the surface of the as-built sample, which act as crack initiation and propagation sites during deformation (Fig. 4a, b) [15]. Therefore, the external defects of the as-built samples induce large roughness on the surface, leading to the degradation of the mechanical properties. The machined specimen exhibited a clean surface with polished traces and some pores (Fig. 4c, d). Meanwhile, as shown in Fig. 4e, f, the severe impact of the WC ball during the UNSM treatment changes the surface morphology. The UNSM-treated samples show crumbled traces due to the compression of unmelted powders, while the external defects such as unmelted particles and cracks of the as-built sample were not observed. Although the cracks are not observed in Figs. 4e and f, the cracks may be formed by severe impact and covered by crumbled powder [41]. The cracks by UNSM can act as crack propagation sites and deteriorate the mechanical properties. Consequently, the UNSM treatment effectively leveled the overall surface height by exerting a compressive force on the surface, resulting in improved surface roughness.

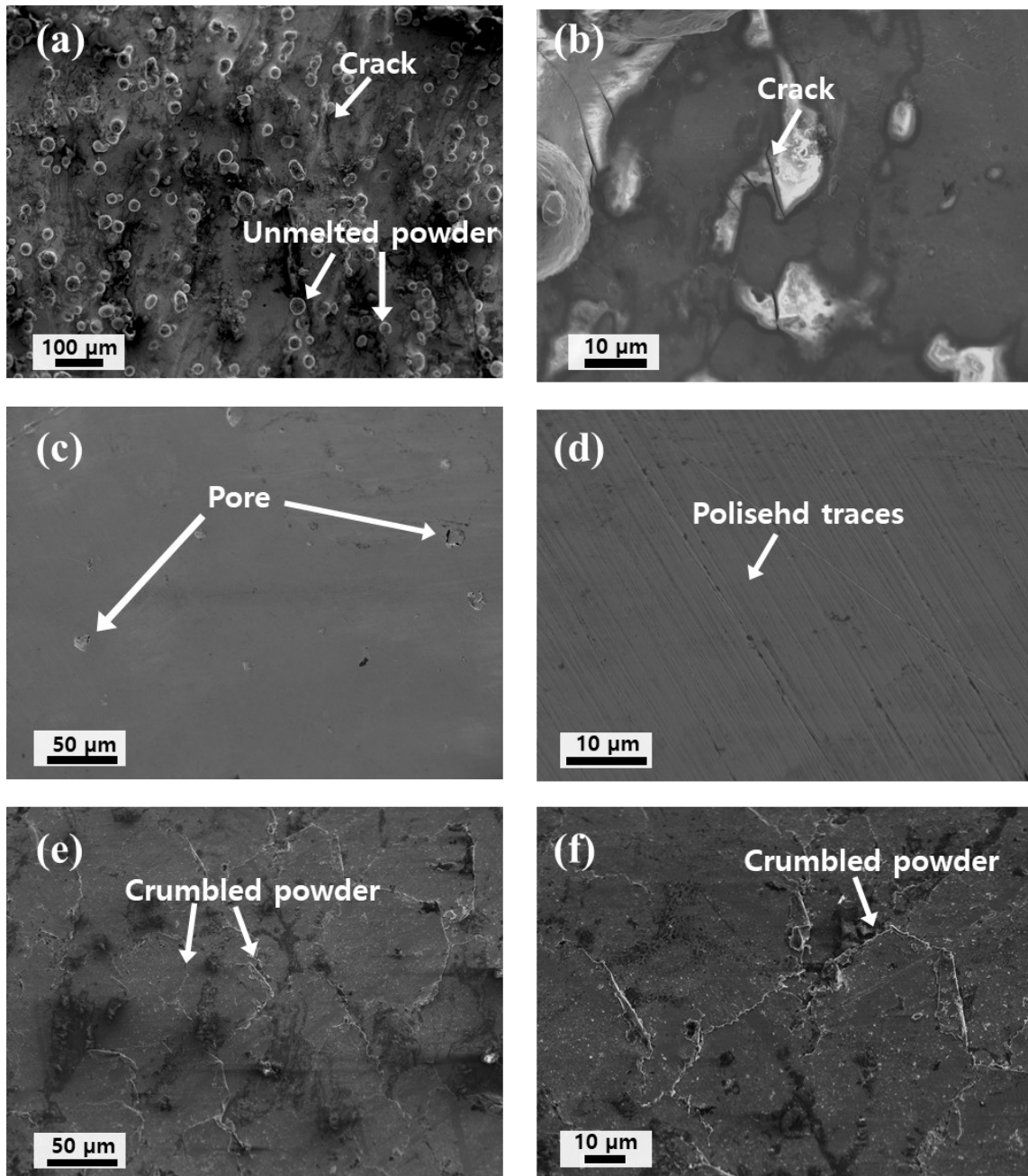


Fig. 4. SEM images of the surfaces for the (a, b) as-built (c, d) as-polished, and (e, f) UNSM-treated samples. (b, d, f) are magnified images of (a, c, e), respectively.

The SEM-BSE cross-section micrographs of the UNSM-treated and untreated LPBF samples are shown in Fig. 5. The LPBF-built samples exhibited a uniform microstructure with pores near the surface. However, as shown in Figures 3 and 5, the subsurface pores which are distributed up to the depth of 200 μm from surface were closed by the severe impact during UNSM treatment. However, the fine pores in the center region are still present after UNSM

treatment. Therefore, UNSM treatment has the pore closure effect up to the depth of 200 μm from the UNSM-treated surface. It is worth noting that the UNSM treatment resulted in significant microstructural changes due to surface severe plastic deformation. Although the UNSM-affected regions exist as gradients, each region was divided with its distinct microstructural characteristics. Region-I, which is the center region of the UNSM-treated samples, contained a similar microstructure to the UNSM-untreated samples. Regions II and III, which are the UNSM-affected regions (approximately 140 μm from the surface), exhibited deformed microstructures with twinning activity. Especially in Region III, a high density of twins and twin bundles are observed.

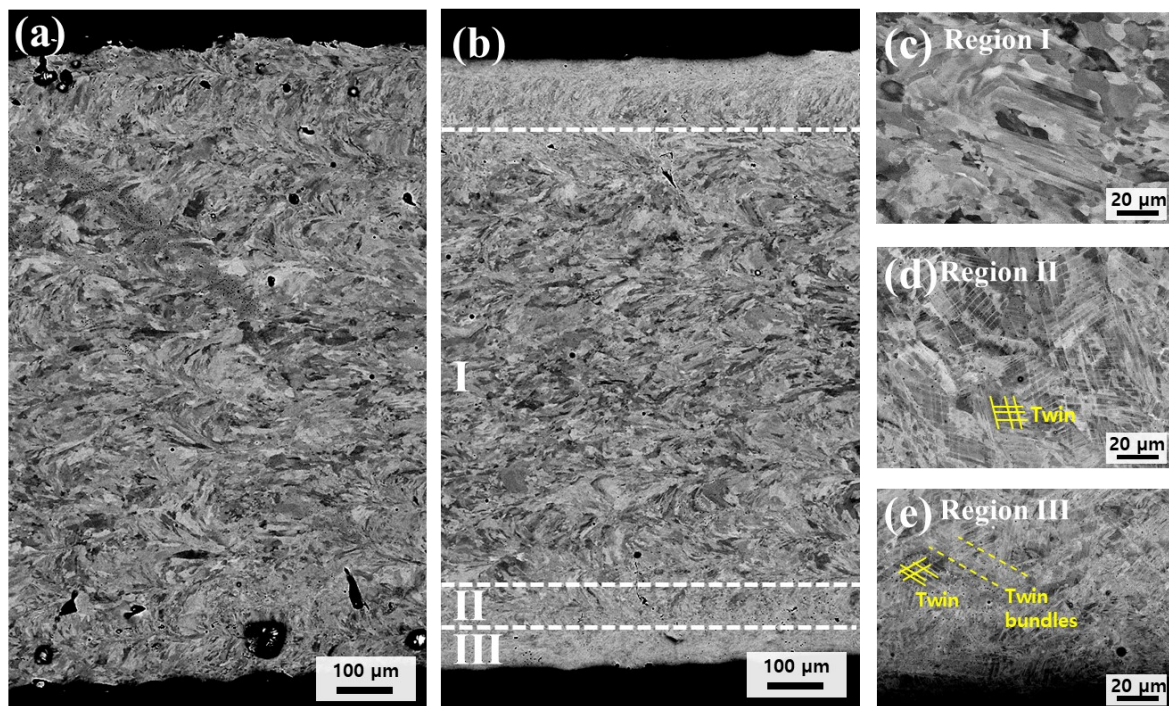


Fig. 5. (a) SEM-BSE cross-section micrographs of the (a) UNSM-untreated and (b) UNSM-treated samples. (c-e) The magnified images of different locations in (b).

The EBSD maps of the UNSM-treated and untreated samples on the normal plane of the X direction are shown in Fig. 6. The maps for the LPBF-built sample reveal a uniform columnar grain morphology with an average grain size of $\sim 19.0 \mu\text{m}$ and a geometrically necessary dislocations (GND) density of $\sim 3.4 \times 10^{13} \text{ m}^{-2}$. The as-polished sample shows a similar microstructure with an average grain size of $\sim 16.8 \mu\text{m}$ and a GND density of $3.5 \times 10^{13} \text{ m}^{-2}$ compared to the as-built samples (Fig. S2) because surface polishing did not affect the

microstructure below the surface. The UNSM treatment induced severe plastic deformation and significant microstructural changes to the base samples. The UNSM-treated regions show a significantly higher GND density than the untreated base samples. The image at high magnification and misorientation plot confirm twinning activity in the UNSM-treated surface region (Fig. 6e). The EBSD image of Fig. 6c exhibits that the map was segmented into bins with a height of 20 μm . Subsequently, GND density and low angle boundary (ρ_{LAGB} , misorientation angle below 15°) fraction were plotted with the distance from the UNSM-treated surface in Fig. 7a and b, respectively. The GND density and ρ_{LAGB} are the highest at the surface, where the UNSM affected severely, and decreased gradually with the distance from the surface until the depth of $\sim 120 \mu\text{m}$. The UNSM treatment develops a gradient layer in the microstructure, which generates a coupling effect for enhanced mechanical properties.

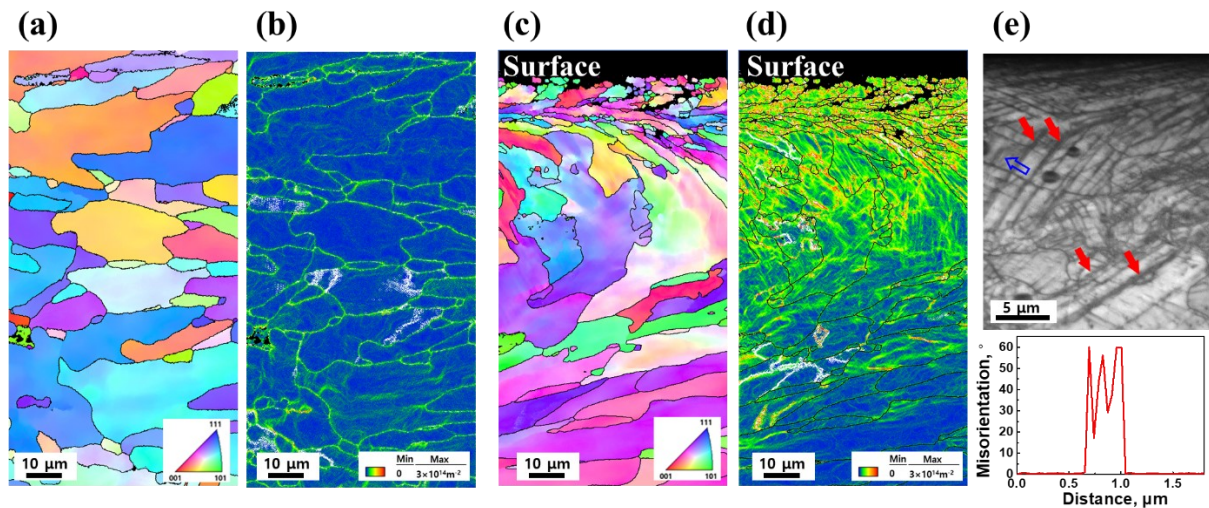


Fig. 6. EBSD images of the (a, b) as-built and (c, d, e) UNSM-treated samples. (a, c) orientation image maps, (b, d) GND density maps, and (e) image quality map at a high magnification near the surface. The red arrow indicates twins and the misorientation plots along the blue arrow.

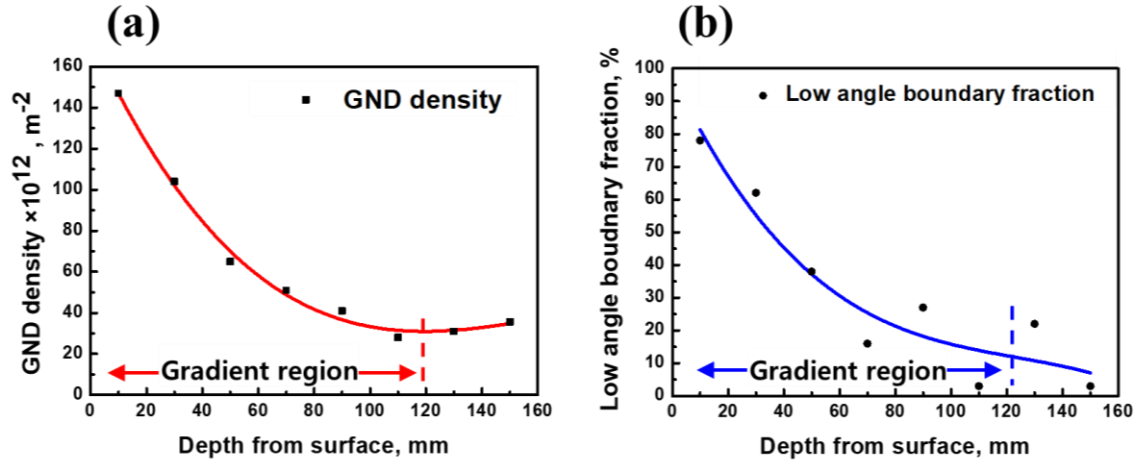


Fig. 7. The plots of (a) GND density variations and (b) low-angle grain boundary fraction variations as a function of distance from the UNSM-treated surface.

XRD spectra of all the samples from 40° to 110° are shown in Fig. 8a. The as-built samples show single FCC phase peaks. The as-polished samples show the main peaks of FCC and minor peaks of BCC. The UNSM-treated samples exhibited the main FCC peaks with the most intense BCC peaks, attributed to the martensite transformation resulting from severe plastic deformation. Furthermore, the UNSM-treated samples show significant peak broadening due to the high lattice microstrain and fine grain size on the surface (Fig. 8b). The full width at half maximum (FWHM) for all samples is given in Fig. 7c. The results of FWHM showed that the sample with the UNSM treatment had the highest value, followed by the samples with polishing, and finally, the sample without post-processing, in order of degree of deformation.

The residual stress measurement results are shown in Fig. 8d. The LPBF-built samples demonstrated a large surface tensile residual stress of ~ 97.3 MPa, which is attributed to thermal gradient, non-uniform shrinkage during solidification, and rapid cooling during the LPBF process [42]. The tensile residual stress on the surface can render it susceptible to cracking and may lead to a brittle deformation mode [43]. Mechanical polishing induces a minor compressive residual stress of ~ 28.8 MPa [44]. Notably, the UNSM-treated samples exhibited significant compressive residual stress of ~ 344.1 MPa. The compressive residual stress layer on the surface contributes to the improvement in mechanical properties by reinforcing the material's gradient structure [45].

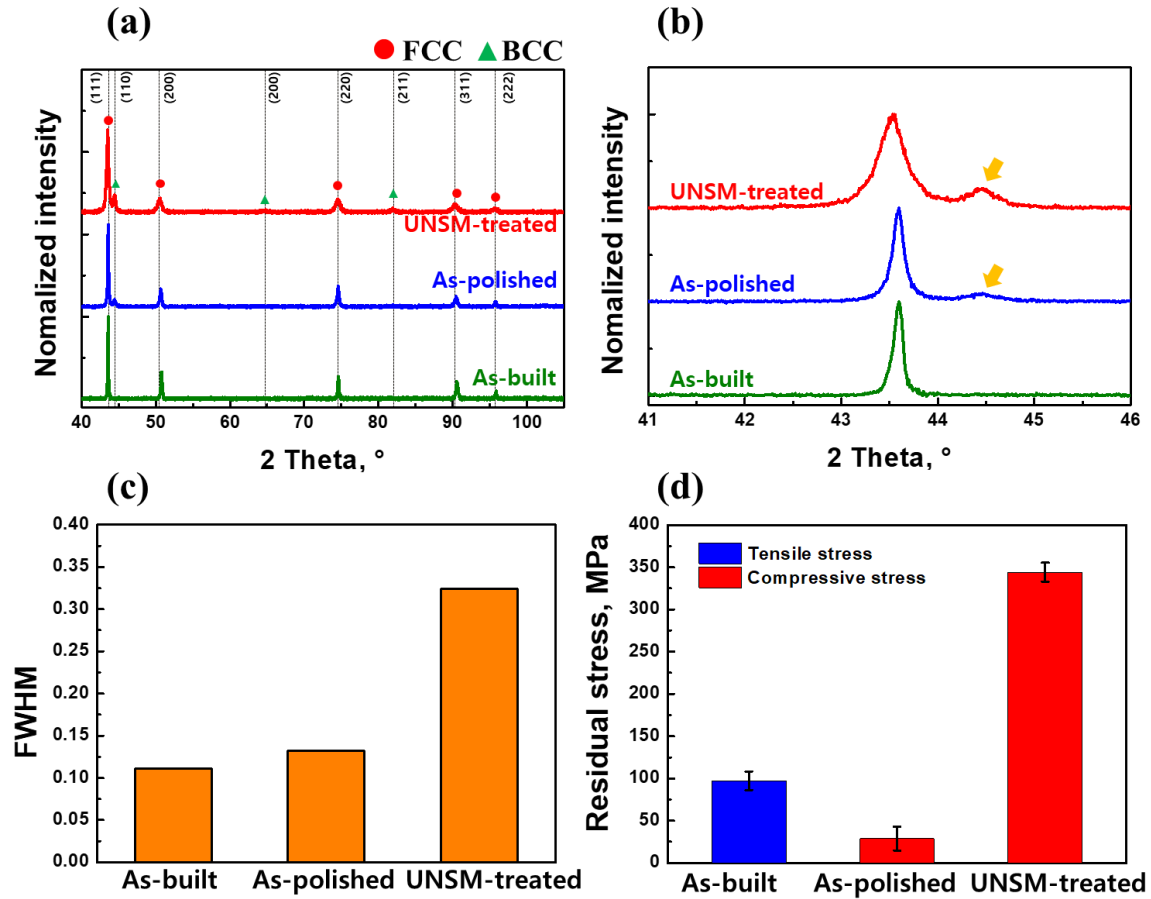


Fig. 8. (a) XRD plots and (b) the magnified image of (a) from 41° to 46° of the present samples. (c) FWHM was calculated from the FCC (111) peak. (d) The residual stress results of the present samples. The yellow arrow in (b) represents the BCC (110) peak.

Figure 9a shows the microhardness profile of the as-built samples before and after the UNSM treatment. The as-built samples exhibited a uniform hardness value of $\sim 262.2 \pm 5.2$ HV. The UNSM treatment resulted in a considerable increase in hardness near the surface, with a peak hardness of $\sim 380.1 \pm 26.2$ HV. Further, the hardness value gradually decreases with distance from the surface, indicating a gradient layer in mechanical properties after UNSM treatment. The depth of the gradient region in the hardness profile was ~ 150 μm , which is consistent with the gradient microstructure layer of ~ 140 μm in Fig. 5b. The high GND evolution, twinning activity, and high LAGB fraction contribute to the gradient layer in mechanical properties.

The engineering stress-strain curves of all the samples are presented in Fig. 9b, and their

tensile properties are summarized in Table 3. As can be seen, the as-built and as-polished samples exhibited similar yield strengths (YS, as-built: 507.9 MPa and as-polished: 504.6 MPa), ultimate tensile strengths (UTS, as-built: 658.5 MPa and as-polished: 652.0 MPa), and uniform elongations (U.El, as-built: 34.7% and as-polished: 34.5%). This indicates that surface polishing did not affect the yield strength and strain hardening under uniform elongation regions. However, the total elongation (T.El) was higher in LPBF samples after polishing (~54.9%) than in the as-built sample (~46.0%) due to post-elongation degradation in the as-built condition. Damage evolution during testing leads to a decrease in load-carrying capacity, which is post-necking elongation regimes [46]. High surface roughness due to unmelted powder and micro-cracks renders it susceptible to cracking [14, 15]. Therefore, easy damage evolution in as-built samples results in degradation of ductility. The UNSM treatment led to a substantial enhancement of yield strength (~189.2 MPa) and ultimate strength (~115.8 MPa) when compared to the non-UNSM treated samples. It is worth noting that the UNSM-treated samples exhibited significant improvement in strength (YS: ~189.2 MPa) with a slight loss of ductility (T.El: ~3.3%) when compared to the as-built samples. Further, post-elongation was the highest in the as-polished sample (~23.7%), followed by UNSM-treated samples (~21.4%), and then the as-built samples (~12.5%). It indicates that the damage evolution was highly suppressed after post-processing. The slight decrease in post-elongation when comparing polished and UNSM-treated samples may attributed to the potential micro-crack during UNSM treatment [41]. As-built contained various crack initiation sites, including surface and volumetric defects. Polishing competently eliminates surface defects such as high surface roughness but is still limited in removing inner defects of subsurface pores. However, the UNSM treatment effectively controlled both inner and outer defects by severe plastic deformation on the surface. Moreover, the coupling effect from the gradient layer contributes to the high strength and ductility combination. Consequently, the prevention of damage evolution and development of gradient structure in the UNSM-treated samples showed an excellent strength-ductility combination.

The strain hardening rate (SHR) curves are plotted in Fig. 9c. The non-UNSM-treated samples exhibited a higher SHR curve than the UNSM-treated sample. Saturated strain hardening of the UNSM-treated surface decreases strain hardening ability, leading to a decrease in uniform elongation. The as-built and as-polished samples show similar strain-hardening behavior until uniform elongation (i.e., before the interaction point between the true

curve and SHR curve). However, as-built sample shows a drop in strain hardening after necking, which may be attributed to dominant damage evolution in post-elongation region.

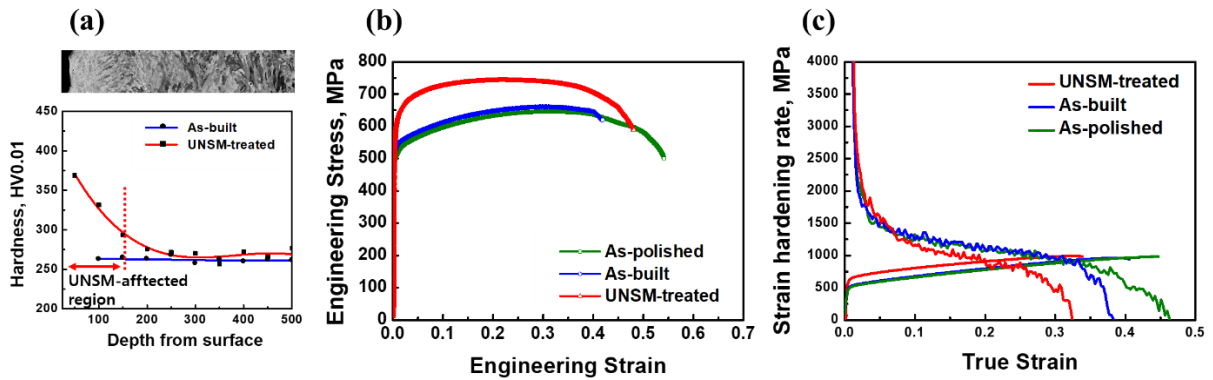


Fig. 9. (a) Vickers microhardness profiles before and after the UNSM treatment. (b) Engineering stress-strain curves and (c) strain hardening rate curves for all the samples.

Table 3. Tensile properties of the present samples.

Samples	Yield strength (YS, MPa)	Uniform elongation (U.El, %)	Ultimate tensile strength (UTS, MPa)	Total elongation (T.El, %)
As-built	507.9±9.4	34.7±4.2	658.5±2.8	47.6±5.0
As-polished	504.6±1.2	34.5±2.7	652.0±4.7	60.5±9.6
UNSM-treated	697.1±103.0	20.6±4.9	774.3±59.7	44.3±7.5

Fig. 10 presents Ashby diagrams comparing the mechanical properties of the current samples with those from published works on 316L stainless steel fabricated by wrought, LPBF, and direct energy deposition (DED). The comparisons of 316L stainless steel are selected to the Ashby diagram with the dominant deformation mechanism of dislocation slip. The data sources for the comparison are listed in Supplementary Reference. The as-built and as-polished samples are located within the typical banana-shaped trend in the diagrams. However, more importantly, the present UNSM-treated alloy with a gradient structure while avoiding built defects shows an excellent combination of strength and ductility.

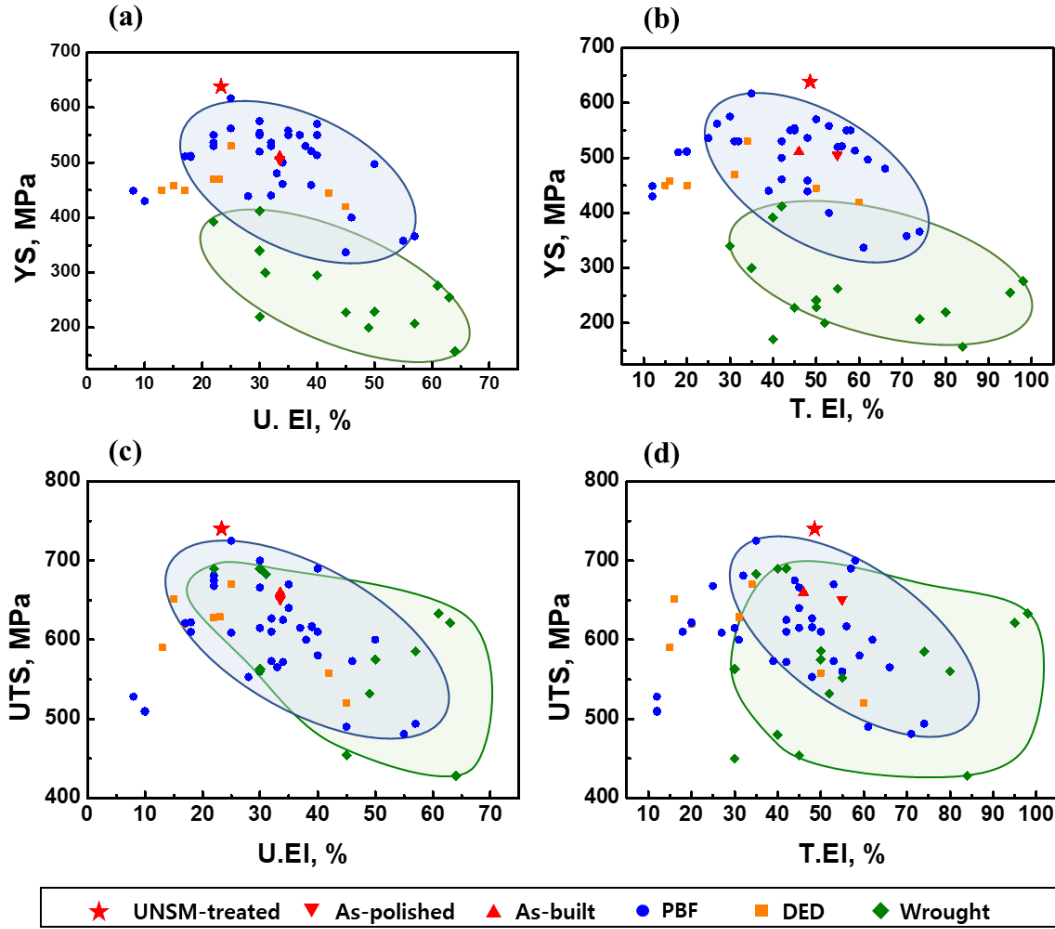


Fig. 10. Ashby diagrams with the comparison of (a) yield strength vs. uniform elongation, (b) yield strength vs. total elongation, (c) ultimate tensile strength vs. uniform elongation, and (d) ultimate tensile strength vs. total elongation.

The gradient features in microstructure and mechanical properties can lead to strength-ductility synergy through substantial HDI strengthening. During the deformation of heterostructured materials, the mechanical incompatibility between the hard and soft domains induces strain gradients at hetero-boundaries [47, 48]. Extra GNDs are accumulated in the interface by strain gradient from mutual constraints [49]. The piled-up GNDs hinder dislocation mobility and generate long-range HDI stress [50, 51]. The applied stress is counterbalanced by HDI stress, which acts in the direction opposite to the applied shear stress, resulting in extra hardening [52]. LUR tests are performed to evaluate the HDI stress during deformation [39]. Figure 11 shows the HDI stress in the UNSM-treated and untreated samples. Interestingly, the fraction of the HDI stress to the flow stress ($\sigma_{\text{HDI}}/\sigma_f$, ~59%) in the UNSM-treated was higher

than that in the non-treated samples ($\sigma_{\text{HDI}}/\sigma_f \sim 54\%$). The development of gradient through the UNSM treatment produces a high number of interfaces of gradient mechanical incompatibility, which leads to a high synergistic effect. It is well reported that the cellular structure by the rapid cooling rate in LPBF, which acts as micro-heterogeneity, results in high HDI stress [53]. However, the cellular boundary is not strong enough to withstand stress concentration by the piled-up GNDs during deformation [54, 55]. More clearly, the increment of flow stress, HDI stress, and effective stress after the UNSM treatment are present in Fig. 11c. The effective stress was calculated by subtracting the HDI stress from the flow stress. The difference in flow stress mainly resulted from a high portion of the HDI stress component, indicating that the HDI stress predominantly contributed to the strengthening of the UNSM-treated samples.

The microstructures of the UNSM-treated and untreated samples, subjected to a true strain of 10%, are presented in Fig. 11c, d. GNDs are accumulated to maintain the lattice continuity in heterostructured materials during the deformation. Notably, significant GNDs are accumulated in the gradient region of the UNSM-treated samples (Fig. 11e). Therefore, the difference in GND density between the initial and 10% strain was higher in the UNSM-treated samples ($\sim 2.5 \times 10^{13} \text{ m}^{-2}$) than in the as-built samples ($\sim 1.4 \times 10^{13} \text{ m}^{-2}$) due to the more heterogeneities in the microstructure of the UNSM-treated samples. Consequently, more prominent GND evolution and HDI stress contribute to superior strength and ductility combination.

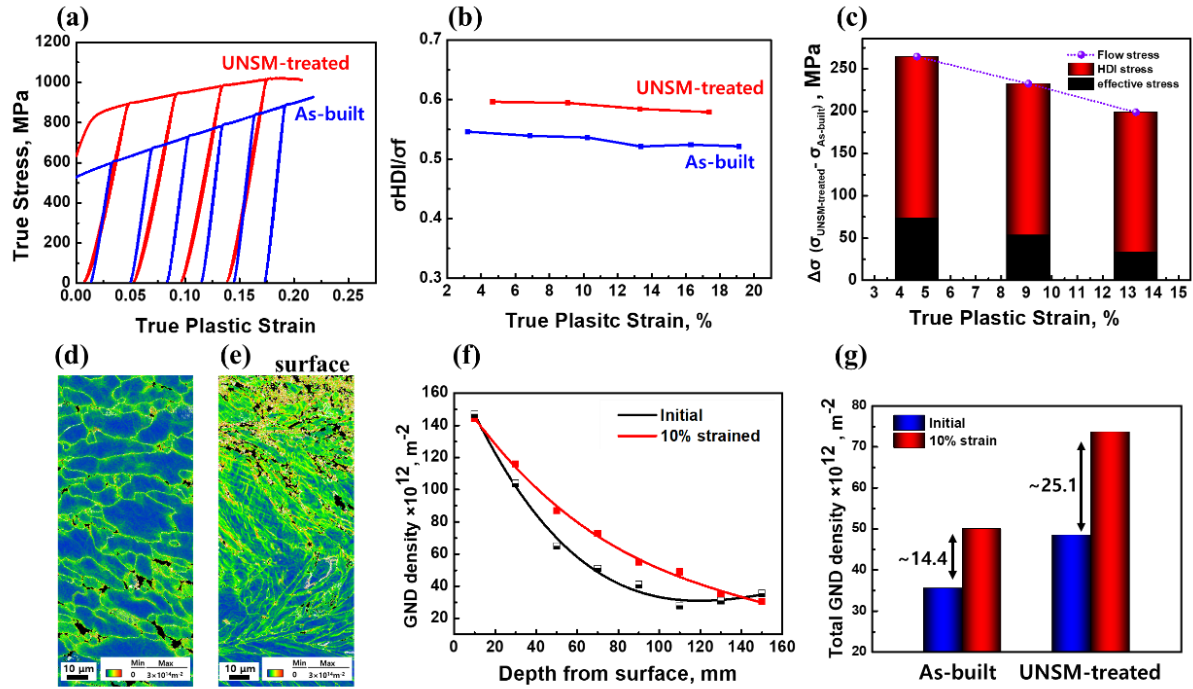


Fig. 11. (a) LUR plots and (b) the fraction of HDI stress to the flow stress plotted with the true plastic strain of the UNSM treated and untreated 316L stainless steel. (c) Stress increment of flow stress, HDI stress, and effective stress before and after the UNSM treatment. GND density maps subjected to a true strain of 10% for the (d) as-built and (e) UNSM-treated samples. (f) GND density plots with the distance from the surface for the initial and deformed UNSM-treated samples. (g) The bar chart showing the total GND density for the UNSM-treated and as-built samples at the initial and deformed states.

The fracture surfaces of the present samples are shown in Fig. 12. All the samples showed fine dimples characterized as ductile fracture features in the center region [56]. A high number of pores are shown in the surface region of the as-built and as-polished samples, which act as crack initiation sites. The UNSM-treated samples showed some flat fractures due to heavily deformed grains in the UNSM-treated surface.

Further, the main advantage of LPBF lies in the production of the part with complex geometries. UNSM process can also be applied to curved shapes [41, 57]. Therefore, it has a high potential to be utilized on complex shapes fabricated by LPBF.

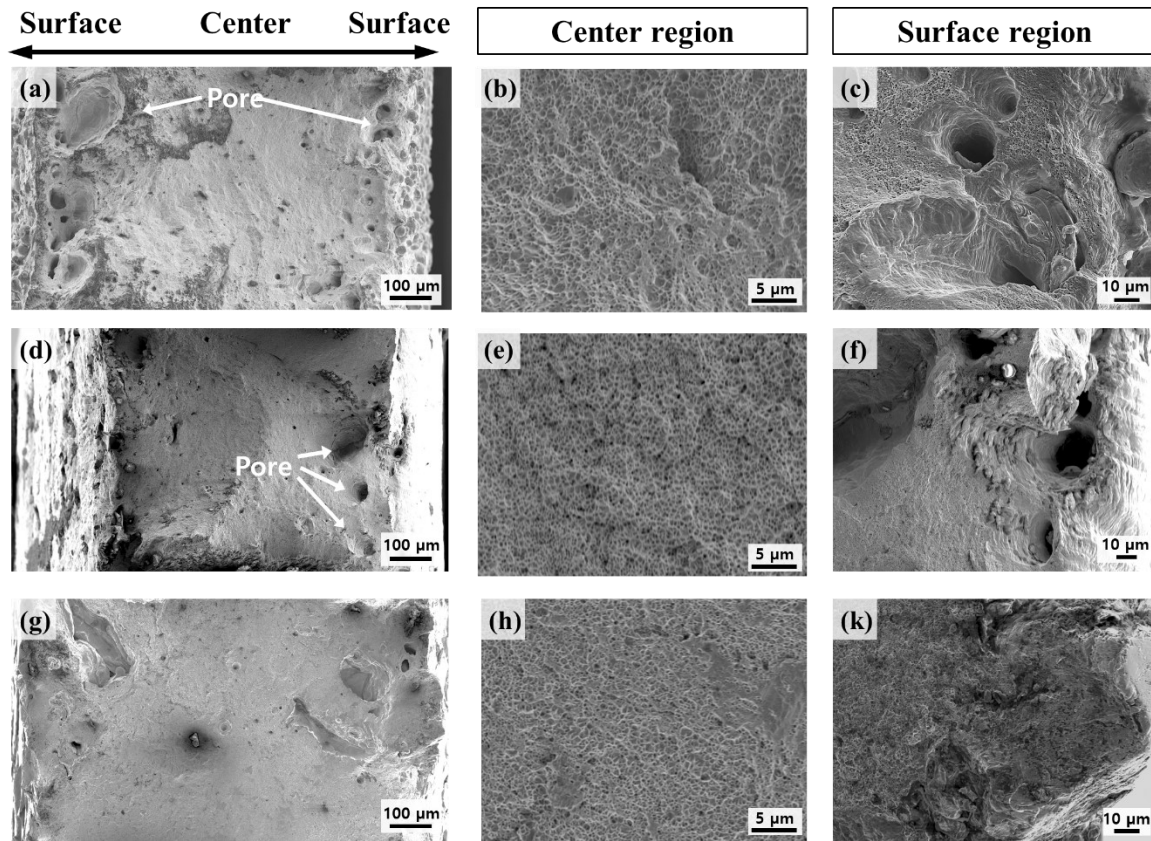


Fig. 12 Fracture surfaces of the (a-c) as-built, (d-f) as-polished, and (g-k) UNSM-treated samples. (b, e, h) represent the center regions, and (c, f, k) represent the surface regions.

4. Conclusion

The laser powder bed fusion (LPBF)-processed 316L stainless steel parts contain defects such as subsurface pores and high surface roughness, which deteriorate mechanical properties. A new approach, ultrasonic nanocrystal surface modification (UNSM), was suggested to control the built defects. The primary conclusions are as follows:

1. The LPBF-processed parts exhibited several building defects, including (i) a high density of pores near the surface, (ii) large surface roughness, and (iii) high tensile residual stress on the surface. These defects, which act as damage evolution sites, lead to a large decrease in the ductility of built parts.
2. The UNSM treatment on built parts effectively controlled building defects through severe external impact on the surface. The LPBF samples treated with the UNSM exhibited notable improvements in microstructure: (i) closure of subsurface pores, (ii) reduced surface

roughness, and (iii) significant compressive residual stress. Further, a gradient layer in microstructure and mechanical properties was developed on the UNSM-treated samples.

3. Even with significant strength enhancement resulting from high deformation on the surface, the UNSM-treated samples retained ductility compared to the as-built samples. Alleviating the trade-off between strength and ductility was achieved through high synergistic hardening from the gradient microstructure and suppression of crack initiation sites by controlled building defects.

This study contributes to broadening the industrial applicability of metal additive manufactured materials by suggesting a new approach to control building defects.

CRedit authorship contribution statement

R.E. Kim: Conceptualization, Methodology, Data curation, Formal analysis, Investigation, Writing – original draft; **S.G. Jeong, H. Ha, D.W. Lee, and A. Amanov:** Investigation; **H.S. Kim:** Conceptualization, Resource, Supervision, Project management, Funding acquisition, Writing – review and editing.

Acknowledgment

This work was supported by the National Research Foundation of Korea (NRF) grant funded by the Korea government (MSIT) (NRF-2022R1A5A1030054 and NRF-2021R1A2C3006662).

References

- [1] W. Choo, M. Ebrahimian, K. Choi, J.H. Kim, Influence of heat treatment on the microstructure and hardness of 17-4ph stainless steel fabricated through direct energy deposition, *Met. Mater. Int.* 29 (2022) 1750-1760, <https://doi.org/10.1007/s12540-022-01333-2>
- [2] A. Khorasani, I. Gibson, J. K. Veetil, A. H. Ghasemi, A review of technological improvements in laser-based powder bed fusion of metal printers, *Int. J. Adv. Manuf. Technol.* 108 (2020) 191-209, <https://doi.org/10.1007/s00170-020-05361-3>.
- [3] J.M. Park, J. Choe, H.K. Park, S. Son, J. Jung, T.-S. Kim, J.-H. Yu, J.G. Kim, H.S. Kim, Synergetic strengthening of additively manufactured (CoCrFeMnNi)₉₉C₁ high-entropy alloy by heterogeneous anisotropic microstructure, *Addit. Manuf.* 35 (2020) 101333, <https://doi.org/10.1016/j.addma.2020.101333>.
- [4] M. Orme, I. Madera, M. Gschweidl, M. Ferrari, Topology optimization for additive manufacturing as an enabler for light weight flight hardware, *Designs* 2 (2018) 51, <https://doi.org/10.3390/designs2040051>
- [5] A.M. Vilardell, A. Takezawa, A. du Plessis, N. Takata, P. Krakhmalev, M. Kobashi, I. Yadroitsava, I. Yadroitsev, Topology optimization and characterization of Ti6Al4V ELI cellular lattice structures by laser powder bed fusion for biomedical applications, *Mater. Sci. Eng. A* 766 (2019) 138330, <https://doi.org/10.1016/j.msea.2019.138330>.
- [6] R.E. Kim, G.M. Karthik, A. Amanov, Y.-U. Heo, S.G. Jeong, G.H. Gu, H. Park, E.S. Kim, D.W. Lee, H.S. Kim, Superior gradient heterostructured alloys fabricated by laser powder bed

- fusion via annealing and ultrasonic nanocrystal surface modification, *Scr. Mater.* 230 (2023) 115422, <https://doi.org/10.1016/j.scriptamat.2023.115422>.
- [7] S.Y. Ahn, E.S. Kim, G.M. Karthik, K.R. Ramkumar, S.G. Jeong, R.E. Kim, G.H. Gu, H.S. Kim, Thickness effect on the microstructures, mechanical properties, and anisotropy of laser-powder bed fusion processed 316L stainless steel, *J. Mater. Sci.* 57 (2022) 18101–18117, <https://doi.org/10.1007/s10853-022-07516-x>
- [8] D. Panov, O. Oreshkin, B. Voloskov, V. Petrovskiy, I. Shishkovsky, Pore healing effect of laser polishing and its influence on fatigue properties of 316L stainless steel parts fabricated by laser powder bed fusion, *Opt. Laser Technol.* 156 (2022) 108535, <https://doi.org/10.1016/j.optlastec.2022.108535>.
- [9] S. Chowdhury, N. Yadaiah, C. Prakash, S. Ramakrishna, S. Dixit, L.R. Gupta, D. Buddhi, Laser powder bed fusion: a state-of-the-art review of the technology, materials, properties & defects, and numerical modeling, *J. Mater. Res. Technol.* 20 (2022) 2109–2172, <https://doi.org/10.1016/j.jmrt.2022.07.121>.
- [10] F.H. Kim, S.P. Moylan, Literature Review of Metal Additive Manufacturing Defects, National Institute of Standards and Technology, 2018, <https://doi.org/10.6028/nist.Ams.100-16>.
- [11] M.J. Heiden, L.A. Deibler, J.M. Rodelas, J.R. Koepke, D.J. Tung, D.J. Saiz, B.H. Jared, Evolution of 316L stainless steel feedstock due to laser powder bed fusion process, *Addit. Manuf.* 25 (2019) 84–103, <https://doi.org/10.1016/j.addma.2018.10.019>.
- [12] Z. Sun, X. Tan, S.B. Tor, W.Y. Yeong, Selective laser melting of stainless steel 316L with low porosity and high build rates, *Mater. Des.* 104 (2016) 197–204, <https://doi.org/10.1016/j.matdes.2016.05.035>.
- [13] E. Maleki, S. Bagherifard, M. Bandini, M. Guagliano, Surface post-treatments for metal additive manufacturing: progress, challenges, and opportunities, *Addit. Manuf.* 37 (2021) 101619, <https://doi.org/10.1016/j.addma.2020.101619>.
- [14] P. Li, D.H. Warner, J.W. Pegues, M.D. Roach, N. Shamsaei, N. Phan, Towards predicting differences in fatigue performance of laser powder bed fused Ti-6Al-4V coupons from the same build, *Int. J. Fatig.* 126 (2019) 284–296, <https://doi.org/10.1016/j.ijfatigue.2019.05.004>.
- [15] W. Everhart, E. Sawyer, T. Neidt, J. Dinardo, B. Brown, The effect of surface finish on tensile behavior of additively manufactured tensile bars, *J. Mater. Sci.* 51 (2016) 3836–3845, <https://doi.org/10.1007/s10853-015-9702-9>

- [16] T. Yang, T. Liu, W. Liao, H. Wei, C. Zhang, X. Chen, K. Zhang, Effect of processing parameters on overhanging surface roughness during laser powder bed fusion of AlSi10Mg, *J. Manuf. Process.* 61 (2021) 440-453, <https://doi.org/10.1016/j.jmapro.2020.11.030>.
- [17] A. du Plessis, P. Rossouw, Investigation of porosity changes in cast Ti6Al4V rods after hot isostatic pressing, *J. Mater. Eng. Perform.* 24 (2015) 3137-3141, <https://doi.org/10.1007/s11665-015-1580-4>.
- [18] M. Nakatani, H. Masuo, Y. Tanaka, Y. Murakami, Effect of Surface Roughness on Fatigue Strength of Ti-6Al-4V Alloy Manufactured by Additive Manufacturing, *Procedia Struct. Integr.* 19 (2019) 294-30, <https://doi.org/10.1016/j.prostr.2019.12.032>.
- [19] A.A. Akilan, R.K. Enneti, V.K. Balla, S.V. Atre, Effects of Hot Isostatic Pressing on the Properties of Laser-Powder Bed Fusion Fabricated Water Atomized 25Cr7Ni Stainless Steel. *Lubricants*, 10 (2022) 340, <https://doi.org/10.3390/lubricants10120340>.
- [20] J. W. Bae, P. Asghari-Rad, A. Amanov, H. S. Kim, Gradient-structured ferrous medium-entropy alloys with enhanced strength-ductility synergy by ultrasonic nanocrystalline surface modification, *Mater. Sci. Eng. A*, 826 (2021) 141966, <https://doi.org/10.1016/j.msea.2021.141966>.
- [21] J. Oh, H. D. Park, M. Gwak, J. Lee, S. Son, A. Amanov, H. S. Kim, J. B. Seol, H. Sung, J. G. Kim, Mechanical property enhancement in gradient structured aluminum alloy by ultrasonic nanocrystalline surface modification, *Mater. Sci. Eng. A*, 812 (2021) 141101, <https://doi.org/10.1016/j.msea.2021.141101>.
- [22] J.G. Kim, J.H. Moon, A. Amanov, H.S. Kim, Strength and ductility enhancement in the gradient structured twinning-induced plasticity steel by ultrasonic nanocrystalline surface modification, *Mater. Sci. Eng. A* 739 (2019) 105-108, <https://doi.org/10.1016/j.msea.2018.10.045>.
- [23] R. Liu, S. Yuan, N. Lin, Q. Zeng, Z. Wang, Y. Wu, Application of ultrasonic nanocrystal surface modification (UNSM) technique for surface strengthening of titanium and titanium alloys: a mini review, *J. Mater. Res. Technol.* 11 (2011) 351-377, <https://doi.org/10.1016/j.jmrt.2021.01.013>.
- [24] X.J. Cao, Y.S. Pyoun, R. Murakami, Fatigue properties of a S45C steel subjected to ultrasonic nanocrystal surface modification, *Appl. Surf. Sci.* 256 (2010) 6297-6303, <https://doi.org/10.1016/j.apsusc.2010.04.007>.

- [25] C. Ma, M. T. Andani, H. Qin, N. S. Moghaddam, H. Ibrahim, A. Jahadkbar, A. Amerinatanzi, Z. Ren, H. Zhang, G. L. Doll, Y. Dong, M. Elahinia, C. Ye, Improving surface finish and wear resistance of additive manufactured nickel-titanium by ultrasonic nano-crystal surface modification, *J. Mater. Process. Technol.* 249 (2017) 433-440, <https://doi.org/10.1016/j.jmatprotec.2017.06.038>.
- [26] A. Amanov, I.-S. Cho, Y.-S. Pyun, Microstructural evolution and surface properties of nanostructured Cu-based alloy by ultrasonic nanocrystalline surface modification technique, *Appl. Surf. Sci.* 388 (2016) 185-195, <https://doi.org/10.1016/j.apsusc.2016.01.237>.
- [27] G.M. Karthik, Y. Kim, E.S. Kim, A. Zargaran, P. Sathiyamoorthi, J.M. Park, S.G. Jeong, G.H. Gu, A. Amanov, Gradient heterostructured laser-powder bed fusion processed CoCrFeMnNi high entropy alloy, *Addit. Manuf.* 59 (2022) 103131, <https://doi.org/10.1016/j.addma.2022.103131>.
- [28] Y. Liu, J. Sun, Y. Fu, B. Xu, B. Li, S. Xu, P. Huang, J. Cheng, Y. Han, J. Han, G. Wu, Tuning strength-ductility combination on selective laser melted 316L stainless steel through gradient heterogeneous structure, *Addit. Manuf.* 48 (2021) 102373, <https://doi.org/10.1016/j.addma.2021.102373>.
- [29] R.E. Kim, G.M. Karthik, A. Amanov, Y.-U. Heo, S.G. Jeong, G.H. Gu, H. Park, E.S. Kim, D.W. Lee, H.S. Kim, Superior gradient heterostructured alloys fabricated by laser powder bed fusion via annealing and ultrasonic nanocrystal surface modification, *Scr. Mater.* 230 (2023) 115422, <https://doi.org/10.1016/j.scriptamat.2023.115422>
- [30] Z. Tong, W. Wan, H. Liu, W. Zhou, Y.X. Ye, X. Ren, Combination of annealing and laser shock peening for tailoring microstructure and mechanical properties of laser directed energy deposited CrMnFeCoNi high-entropy alloy, *Addit. Manuf.* 61 (2023) 103345, <https://doi.org/10.1016/j.addma.2022.103345>.
- [31] S.Y. Ahn, D.G. Kim, J.A. Lee, E.S. Kim, S.G. Jeong, R.E. Kim, J. Choe, S.-J. Hong, P. Quang, S. Lee, H.S. Kim, Dynamic compression behavior of CoCrFeMnNi high-entropy alloy fabricated by direct energy deposition additive manufacturing. *J. Alloys Compd.* 960 (2023) 170602, <https://doi.org/10.1016/j.jallcom.2023.170602>.
- [32] J. Zhou, Y. Wang, G. Zhi, L. He, Effect of Laser Power on Anisotropic Microstructure and Mechanical Behavior of Biomedical Ti-35Nb-15Zr (at%) Alloy Fabricated by Laser Powder Bed Fusion, *Met. Mater. Int.* (2023), <https://doi.org/10.1007/s12540-023-01494-8>.

- [33] H.M. Joo, W.C. Kim, Y.J. Kim, Y.C. Jo, M.G. Kang, J.Y. Lee, M.S. Kim, G.B. Kim, S. J. Kim, D.H. Kim, Effect of Laser Power on the Microstructure Evolution and Mechanical Properties of 20MnCr5 Low Alloy Steel Produced by Laser-Based Powder Bed Fusion, *Met. Mater. Int.* 29 (2023) 983-993, <https://doi.org/10.1007/s12540-022-01294-6>.
- [34] A. Saboori, A. Aversa, F. Bosio, E. Bassini, E. Librera, M.D. Chirico, S. Biamino, D. Ugues, P. Fino, M. Lombardi. An investigation on the effect of powder recycling on the microstructure and mechanical properties of AISI 316L produced by Directed Energy Deposition, *Mater. Sci. Eng. A* 766 (2019) 138360, <https://doi.org/10.1016/j.msea.2019.138360>.
- [35] A. Amanov, Effect of local treatment temperature of ultrasonic nanocrystalline surface modification on tribological behavior and corrosion resistance of stainless steel 316L produced by selective laser melting, *Surf. Coat.* 398 (2020) 126080, <https://doi.org/10.1016/j.surfcoat.2020.126080>.
- [36] G.M. Karthik, E.S. Kim, P. Sathiyamoorthi, A. Zargaran, S.G. Jeong, R. Xiong, S.H. Kang, J.-W. Cho, H.S. Kim, Delayed deformation-induced martensite transformation and enhanced cryogenic tensile properties in laser additive manufactured 316L austenitic stainless steel, *Addit. Manuf.* 47 (2021) 102314, <https://doi.org/10.1016/j.addma.2021.102314>.
- [37] T. Reiber, J. Rudesheim, M. Weigold, E. Abele, J. Musekamp, M. Oechsner, Influence of contour scans on surface roughness and pore formation using Scalmalloy manufactured by laser powder bed fusion (PBF-LD), *Mater. Sci. Eng. C* 52 (2021) 468–481, <https://doi.org/10.1002/mawe.202000287>.
- [38] M. Yang, Y. Pan, F. Yuan, Y. Zhu, X. Wu, Back stress strengthening and strain hardening in gradient structure, *Mater. Res. Lett.* 4 (2016) 145-151. <https://doi.org/10.1080/21663831.2016.1153004/>
- [39] A. Plessis, Effects of process parameters on porosity in laser powder bed fusion revealed by X-ray tomography, *Addit. Manuf.* 30 (2019) 100871. <https://doi.org/10.1016/j.addma.2019.100871>.
- [40] N.T. Aboulkhair, N.M. Everitt, I. Ashcroft, C. Tuck, Reducing porosity in AlSi10Mg parts processed by selective laser melting. *Addit. Manuf.* 1–4 (2014) 77–8, <https://doi.org/10.1016/j.addma.2014.08.001>.
- [41] D. Bae, S. Park, J.B. Seol, D.J. Lee, A. Amanov, H. Sung, J.G. Kim, Microstructural evolution and mechanical properties of laser-powder bed fusion processed 316L stainless steel

with an ultrasonic-nanocrystalline surface modification, *Mater. Sci. Eng. A* 862 (2023) 144436, <https://doi.org/10.1016/j.msea.2022.144436>.

[42] N.C. Levkulich, S.L. Semiatin, J.E. Gockel, J.R. Middendorf, A.T. DeWald, N.W. Klingbeil, The effect of process parameters on residual stress evolution and distortion in the laser powder bed fusion of Ti-6Al-4V, *Addit. Manuf.* 28 (2019) 475-484, <https://doi.org/10.1016/j.addma.2019.05.015>.

[43] X.R. Wu, The effect of welding residual stress on brittle fracture of plates with surface cracks, *Eng. Fract. Mech.* 19 (1984) 427-439, [https://doi.org/10.1016/0013-7944\(84\)90003-1](https://doi.org/10.1016/0013-7944(84)90003-1).

[44] J. Everaerts, E. Salvati, A.M. Korsunsky, Nanoscale Depth Profiling of Residual Stresses Due to Fine Surface Finishing, *Adv. Mater. Interfaces* 6 (2019) 1900947, <https://doi.org/10.1002/admi.201900947>.

[45] M.-X. Yanga, R.-G. Lib, P. Jianga, F.-P. Yuan, Y.-Do. Wang, Y.-T. Zhu, X.-L. Wu, Residual stress provides significant strengthening and ductility in gradientstructured materials, *Mater. Res. Lett.* 7 (2019) 433-438, <https://doi.org/10.1080/21663831.2019.1635537>.

[46] J.-B. Kim, J.W. Yoon, Necking behavior of AA 6022-T4 based on the crystal plasticity and damage models, *Int. J. Plast.* 73 (2015) 3-23, <https://doi.org/10.1016/j.ijplas.2015.06.013>.

[47] R.E. Kim, E.S. Kim, G.M. Karthik, G.H. Gu, S.Y. Ahn, H. Park, J. Moon, H.S. Kim, Heterostructured alloys with enhanced strength-ductility synergy through laser-cladding, *Scr. Mater.* 215 (2022) 114732, <https://doi.org/10.1016/j.scriptamat.2022.114732>.

[48] Y. Zhu, K. Ameyama, P.M. Anderson, I.J. Beyerlein, H. Gao, H.S. Kim, E. Lavernia, S. Mathaudhu, H. Mughrabi, R.O. Ritchie, N. Tsuji, X. Zhang, X. Wu, Heterostructured materials: superior properties from hetero-zone interaction, *Mater. Res. Lett.* 9 (2021) 1-31, <https://doi.org/10.1080/21663831.2020.1796836>.

[49] R.E. Kim, G.H. Gu, H. Kwon, S.Y. Ahn, J. Kwon, J.A. Lee, Y.T. Choi, M.H. Seo, H.S. Kim, Role of synergistic hardening and damage evolution on the stretchability of Al1050/steel/Al1050 sheets, *J. Mater. Res. Technol.* 21 (2022) 3514-3525, <https://doi.org/10.1016/j.jmrt.2022.10.143>

[50] R.E. Kim, J. Moon, E.S. Kim, J. Lee, H.S. Kim, Surface heterostructuring of laser-clad 316L stainless steel through texture-driven deformation twinning, *Scr. Mater.* 221 (2022) 114989, <https://doi.org/10.1016/j.scriptamat.2022.114989>.

- [51] Y. Kim, J. Jung, H.K. Park, H.S. Kim, Importance of Microstructural Features in Bimodal Structure–Property Linkage, *Met. Mater. Inter.* 29 (2023) 53-58. <https://doi.org/10.1007/s12540-022-01200-0>.
- [52] X. Wu, Y. Zhu, Heterogeneous materials: a new class of materials with unprecedented mechanical properties, *Mater. Res. Lett.* 5 (2017) 527-532, <https://doi.org/10.1080/21663831.2017.1343208>
- [53] G.M. Karthik, H.S. Kim, Heterogeneous aspects of additive manufactured metallic parts: a review, *Met. Mater. Int.* 27 (2021) 1-39, <https://doi.org/10.1007/s12540-020-00931-2>
- [54] D. Kong, C. Dong, X. Ni, Z. Liang, C. Man, X. Li, Hetero-deformation-induced stress in additively manufactured 316L stainless steel, *Mater. Res. Lett.* 8 (2020) 10, <https://doi.org/10.1080/21663831.2020.1775149>
- [55] Z. Li, Z. Li, Z. Tan, D.-B. Xiong, Q. Guo, Stress relaxation and the cellular structure dependence of plastic deformation in additively manufactured AlSi10Mg alloys, *Int. J. Plast.* 127 (2020) 102–111, <https://doi.org/10.1016/j.ijplas.2019.12.003>.
- [56] W.E. Frazier, Metal Additive Manufacturing: A Review, *J. Mater. Eng. Perform.* 23 (2014) 1917–1928, <https://doi.org/10.1007/s11665-014-0958-z>.
- [57] J.H. Moon, S.M. Baek, S. G. Lee, Y. Seong, A. Amanov, S. Lee, H.S. Kim, Effects of residual stress on the mechanical properties of copper processed using ultrasonicnanocrystalline surface modification, *Mater. Res. Lett.* 7 (2019) 3, <https://doi.org/10.1080/21663831.2018.1560370>